JGR Atmospheres

RESEARCH ARTICLE
10.1029/2024JD043209

Microphysical Characteristics of Frontal and Warm Sector Heavy Rainfall Over South China During the Pre-Summer Rainy Season

Hong Wang[1,2], Ming Xue[3], Naigeng Wu[4], Jie He[1], Weiyu Ding[1], and Hua Deng[1]

[1]Guangdong Provincial Key Laboratory of Regional Numerical Weather Prediction, Guangzhou Institute of Tropical and Marine Meteorology, China Meteorological Administration, Guangzhou, China, [2]Key Laboratory of Mesoscale Severe Weather, Ministry of Education and School of Atmospheric Sciences, Nanjing University, Nanjing, China, [3]Center for Analysis and Prediction of Storms and School of Meteorology, University of Oklahoma, Norman, OK, USA, [4]Guangdong Provincial Meteorological Observatory, Guangzhou, China

Key Points:

- Frontal convection has a stronger intensity and larger raindrop size than warm sector convection, although their maritime properties
- Stronger wind shear and more supercooled liquid water may promote storm organization and enhance ice processes in the frontal heavy rainfall
- Warm rain processes dominate the rainfall formation in both frontal and warm sector convection especially coalescence

Correspondence to:

M. Xue,
mxue@ou.edu

Citation:

Wang, H., Xue, M., Wu, N., He, J., Ding, W., & Deng, H. (2025). Microphysical characteristics of frontal and warm sector heavy rainfall over South China during the pre-summer rainy season. *Journal of Geophysical Research: Atmospheres*, *130*, e2024JD043209. https://doi.org/10.1029/2024JD043209

Received 19 DEC 2024
Accepted 8 MAY 2025

Author Contributions:

Conceptualization: Hong Wang, Ming Xue
Data curation: Naigeng Wu, Hua Deng
Investigation: Hua Deng
Methodology: Hong Wang, Naigeng Wu, Weiyu Ding
Software: Jie He
Validation: Weiyu Ding
Visualization: Jie He
Writing – original draft: Hong Wang
Writing – review & editing: Ming Xue, Naigeng Wu

Abstract Two distinct types of precipitation—frontal heavy rainfall (FR) and warm sector heavy rainfall (WR)—frequently occur in South China during early summer (April–June). FR and WR are produced within different environmental conditions, but their microphysical differences and the possible underlying causes remain unclear. We use polarimetric radar observations and the ERA5 reanalysis data to investigate the microphysical properties of convective cells (CCs) in FR and WR. Overall, both frontal and warm sector CCs produce maritime-type convective rain, but FR events exhibit stronger convection intensity, larger raindrop sizes, and higher rain rates than WR events. The larger reflectivity above the freezing level and the higher occurrence frequency of large-sized graupel in FR suggest more active riming process, which might be partly attributed to its stronger dynamic conditions (i.e., larger 0–3 km storm relative helicity and stronger 0–6 km shear) and higher supercooled liquid water content. Collisional coalescence serves as the primary growth mechanism for raindrops in both types of CCs below the melting layer. However, in frontal CCs having the top 10 percentile mass-weighted mean raindrop diameters oversized raindrops undergo breakup. The ratio of ice and liquid water contents indicates that warm rain processes play a key role in the formation of rainfall particularly in WR. These findings provide new insights into the microphysical characteristics of heavy rainfall in the tropical monsoon region of South China.

Plain Language Summary Heavy rainfall contributes substantially to the global precipitation and could trigger hazardous events such as flash floods and landslides. In South China, frontal heavy rainfall (FR) and warm sector heavy rainfall (WR) are two predominant types of precipitation during early summer (April–June). However, the microphysical differences between FR and WR remain poorly understood. To investigate their convective and the microphysical differences, we analyze 3-year, high-resolution polarimetric radar observations, lightning flashes from the Guangdong–Hongkong–Macau lightning mapping system and the fifth-generation European Centre for Medium-Range Weather Forecasts reanalysis (ERA5, which provides synoptic-scale features and soundings) over South China. Results show that FR has a stronger intensity and larger raindrop size than that of WR although their maritime properties. Warm rain processes, especially coalescence, play a dominant role in the formation of both FR and WR.

1. Introduction

South China is typically defined as the region spanning from the Nanling Mountains to the South China Sea (Figure 1) characterized by a complex underlying terrain surface. During the rainy season, this region is influenced by the South China Sea monsoon with strong air-sea-land interactions (Ding et al., 2004). Consequently, South China ranks among the rainiest regions globally and is frequently subject to intense rainfall events across various timescales (Luo et al., 2020). Half of the annual precipitation occurs between April and mid-June, which is commonly known as the pre-summer rainy season in South China (PRSC, Luo et al., 2017). Based on the dominant synoptic-scale weather systems that they occur within, most of the heavy rainfall events during the PRSC can be broadly categorized into two types: frontal heavy rainfall (FR) and warm sector heavy rainfall (WR). WR occurs ahead of a front (>200 km) in the warm sector with weak synoptic or mesoscale forcing (Huang, 1986; Liu et al., 2019; Wu et al., 2020). In contrast, FR is typically associated with strong synoptic or mesoscale forcing such as that of a cold front. In this study, the scope of the FR is expanded to also include cases in which the forcing

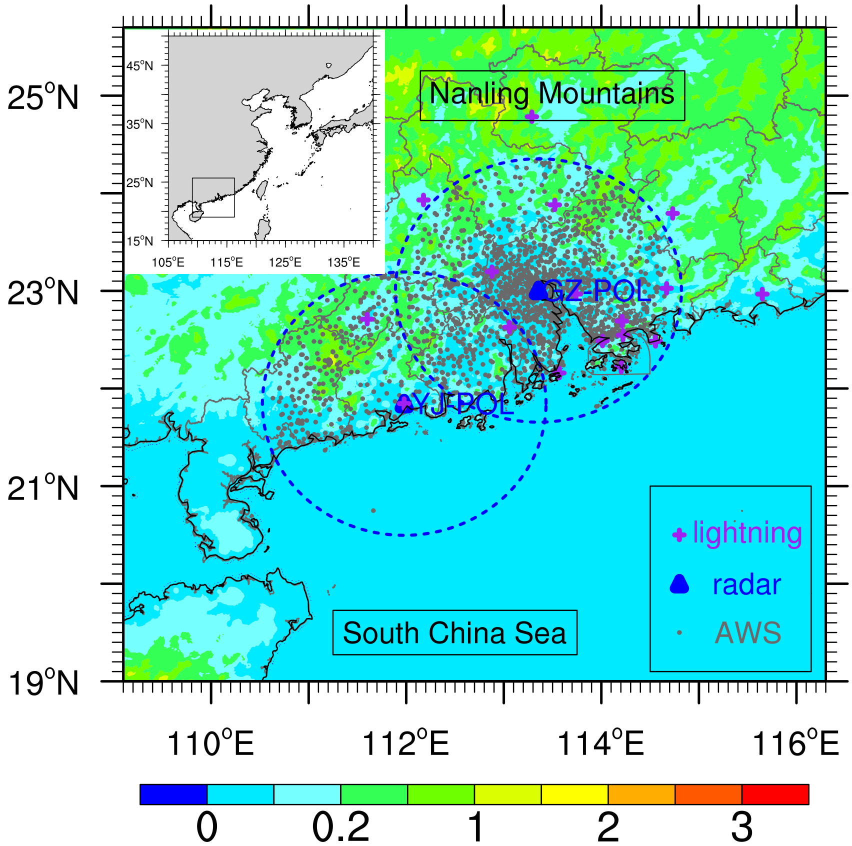

Figure 1. Locations of two S-band radars (triangles), lightning mapping stations (crosses) and automatic weather station stations (gray dots) and the topography (shading; units: km) over South China. The blue dashed circles represent the 150 km range of GZ-POL and YJ-POL radars.

systems involve synoptic or mesoscale shear line and low vortex. Despite some variability in their specific features, the FR cases share the common characteristic of strong forcing leading to their classification as strongly forced rainfall. For simplicity, we refer to this category of cases as FR in this paper.

Both FR and WR can cause flash floods and landslides. Previous studies have offered valuable insights into various phenomena and processes associated with the heavy rainfall over the PRSC especially the differences in dynamic and thermodynamic conditions between FR and WR (Huang, 1986; Luo et al., 2017; Zhang et al., 2011; Zhou et al., 2003). FR is primarily governed by dynamic forcing of synoptic-scale and mesoscale systems, such as fronts, shear lines, and low-level jets at 850–700 hPa (Du & Chen, 2018; Liu et al., 2020). In contrast, WR is usually linked to wind speed convergence near the coastline (Chen et al., 2014), land-sea contrast (Wu et al., 2020), warm humid southerly oceanic flow within the planetary boundary layer (Zhong et al., 2019), and the localized orography (Xu et al., 2018).

Accurate prediction of precipitation during PRSC is challenging especially for WR. As a key component of numerical weather prediction models, microphysics parameterization requires a good understanding of the cloud microphysics of precipitation (Kretzschmar et al., 2020). FR and WR tend to have significantly different dynamic forcing and thermodynamic environments, which can lead to different microphysical characteristics (Han et al., 2021). A comprehensive analysis of microphysics characteristics of heavy rainfall events in the PRSC can contribute to the improvement of microphysics parameterization schemes and precipitation prediction.

Due to the integrated effects over the size distributions, the drop size distributions (DSDs) of hydrometeors provide critical insights into various microphysics processes (Ryzhkov & Zrnic, 2019; Zhang, 2016; Zhao et al., 2019). Because polarimetric radar variables, including radar reflectivity factor for horizontal polarization Z_H, differential reflectivity Z_{DR}, specific differential phase K_{DP}, and co-polar cross-correlation coefficient ρ_{HV}, are DSD-weighted integral parameters (Kumjian, 2013), DSD-related quantities and parameters, such as mass-weighted mean diameter D_m, logarithmic normalized intercept parameter $\log_{10}N_w$, liquid water content LWC, and ice water content IWC, can be retrieved from these polarimetric radar variables (Cao et al., 2013; Huang et al., 2019; Zhang et al., 2001).

Studies (Bringi et al., 2003; Huang et al., 2023; Kneifel & Moisseev, 2020; Yu et al., 2022) have used polarimetric radar measurements combined with disdrometer observations to analyze the temporal and spatial variations of DSDs across different precipitation and regions. Based on $\log_{10}N_w$ and D_m from various climatic regimes, Bringi et al. (2003) classified convective precipitation into maritime type ($D_m \approx$ 1.5–1.75 mm, $\log_{10}N_w \approx$ 4–4.5) and continental type ($D_m \approx$ 2–2.75 mm, $\log_{10}N_w \approx$ 3–3.5). The retrieved convective DSD of rain during Meiyu season in East China has a maritime characteristic in which warm rain processes play the dominant role (Chen et al., 2019; Wen et al., 2020). Observations from Okinawa, Japan have also confirmed that the rain DSD in Meiyu convection is close to that of maritime type rainfall (Oue et al., 2011).

The dual-polarization upgrade of the operational S-band weather radars in Guangdong Province provides an opportunity to analyze the microphysical features of heavy rainfall over South China (Liu et al., 2018; Wang et al., 2019). Han et al. (2021) documented a case in which FR and WR coexisted, reporting that WR exhibited stronger convection intensity and larger raindrop sizes than FR. Yu et al. (2022) carried out a statistical study of extreme precipitation in South China using 2-year S-band polarimetric radar observations and found most extreme precipitation events (∼75%) were dominated by coalescence processes below the melting layer. Huang et al. (2023) found that the extreme precipitation events in the mountainous regions of South China produced larger volumes of rainfall with higher Z_H values above the freezing level and higher lightning flash rates than that in urban areas corresponding to more active riming processes. However, there have been few microphysical studies comparing FR and WR during the PRSC especially those based on long-term radar observations.

In this study, we utilize 3 years of polarimetric radar data combined with observations from surface automatic weather stations (AWSs) and lightning sensors to investigate the characteristics of FR and WR during the PRSC. Several questions will be addressed: (a) what are the differences between FR and WR in terms of precipitation, convective intensity, and synoptic-scale environment? (b) What are their microphysical characteristics and their differences? (c) What are the microphysical processes, and how are they related to the thermodynamic and dynamic environmental conditions? As a consequence, the remainder of this paper is organized as follows. Section 2 details the procedures used to process the radar data. Section 3 examines the weather situation, convective intensity, and precipitation. The differences of microphysics between FR and WR are presented in Section 4 and a discussion and conclusions are given in Section 5.

2. Data and Methods

2.1. Data

We analyze the microphysical properties of heavy rainfall along the South China coast and in the nearby inland areas (Figure 1, within the blue dashed circles), focusing on two types of typical heavy precipitation (FR and WR) during the PRSC. The observation data sets include the 6-min accumulated precipitation measurements from over 1,700 AWSs, lightning flash data from the Guangdong-Hongkong-Macau lightning mapping system, and S-band polarimetric radar data from Guangzhou and Yangjiang (marked as GZ-POL and YJ-POL in Figure 1) in the Pearl River Delta region.

The measurements from GZ-POL and YJ-POL radars are the most important data in this study. The radar systems are dual-polarization-upgraded WSR-98D radars similar in hardware and software to the polarimetric WSR-88D radars of the U.S. National Weather Service. They operate at 10-cm wavelength with a beam width of 0.92° and a gate resolution of 250 m. The radars perform nine elevation scans (0.5°, 1.5°, 2.4°, 3.3°, 4.3°, 6.0°, 9.9°, 14.6°, and 19.5°) with a temporal resolution of 6 min.

All the polarimetric observations (Z_H, Z_{DR}, K_{DP}, and ρ_{HV}) are screened to minimize biases from the non-meteorological particles. The data processing includes nonstandard blockage mitigation, threshold checking, and high-frequency noise filtering. The radar data in polar coordinates are mapped onto a Cartesian grid with a horizontal spacing of 1 km and a vertical spacing of 0.5 km using the 88D2ARPS software from the Center for Analysis and Prediction of Storms. More details on data processing and quality control of the polarimetric radar measurements can be found by Wang et al. (2018).

The synoptic-scale features are analyzed using the fifth-generation European Centre for Medium-Range Weather Forecasts reanalysis (ERA5, Hersbach et al., 2018) data, which have been widely used in weather and climate research in China (Jiang et al., 2019; Xu et al., 2022). Additionally, environmental sounding parameters and derived water vapor quantities are also calculated using the ERA5 data set.

2.2. Retrieval of the Raindrop Size Distribution

Raindrop Size Distribution (RSD) is key in quantitative analysis of microphysical characteristics of heavy rainfall. A three-parameter gamma function is widely used to characterize the RSD:

$$N(D) = N_0 D^{\mu} \exp(-\Lambda D), \tag{1}$$

where N_0 ($\mathrm{mm^{-1}\ m^{-3}}$) is the number concentration parameter, μ is the distribution shape parameter, and Λ ($\mathrm{mm^{-1}}$) is the slope parameter. Based on the statistics of RSD observations, Zhang et al. (2001) found that μ and Λ follow a quadratic relation. The constrained gamma model is therefore established using the μ–Λ relationship to reduce the number of independent parameters from three to two in RSD. The μ–Λ relationship documented by Zhang (2016) is adopted in this study. For convective cells (CCs) with $K_{\mathrm{DP}} > 0.3°\ \mathrm{km^{-1}}$, the quantitative precipitation estimation algorithm $R(K_{\mathrm{DP}})$ from Ryzhkov et al. (2005) is employed, whereas Equation 2 from Wang et al. (2019) is used in other situations. The LWC is retrieved from Z_{H} and Z_{DR} according to Equation 4 from Zhang (2016). Fitting results of D_{m} and Z_{DR} in Equation 5 is used to calculate D_{m}. Details of the retrieval algorithms have been reported previously by Wang et al. (2019).

$$R = 0.0113Z \times 10^{\left(-0.0533Z_{\mathrm{DR}}^3 + 0.382Z_{\mathrm{DR}}^2 - 1.175Z_{\mathrm{DR}}\right)}\ K_{\mathrm{DP}} \le 0.3°\ \mathrm{km^{-1}}; \tag{2}$$

$$R = 47.3{K_{\mathrm{DP}}}^{0.791} K_{\mathrm{DP}} > 0.3°\ \mathrm{km^{-1}}; \tag{3}$$

$$\mathrm{LWC} = 1.023 \times 10^{-3} Z \times 10^{\left(-0.0742Z_{\mathrm{DR}}^3 + 0.511Z_{\mathrm{DR}}^2 - 1.511Z_{\mathrm{DR}}\right)}; \tag{4}$$

$$D_{\mathrm{m}} = 0.7218 \times Z_{\mathrm{DR}} + 0.955; \tag{5}$$

$$N_{\mathrm{w}} = \frac{4^4}{\pi \rho_w}\left(\frac{\mathrm{LWC}}{D_{\mathrm{m}}^4}\right). \tag{6}$$

Here, Z is in linear units ($\mathrm{mm^6\ m^{-3}}$, $Z = 10^{Z_H/10}$), and Z_{DR} and K_{DP} are in dB and $°\ \mathrm{km^{-1}}$, respectively. Variables R, LWC, D_{m}, and N_{w} are in units of $\mathrm{mm\ h^{-1}}$, $\mathrm{g\ m^{-3}}$, mm and $\mathrm{mm^{-1}\ m^{-3}}$, respectively. The measurement errors for Z_{H} and Z_{DR} in well-calibrated S-band radars are typically 1 and 0.2 dB, respectively. The power-law statistical uncertainties of D_{m} and LWC are approximately 0.15 mm and 0.8 $\mathrm{g\ m^{-3}}$.

2.3. Hydrometeor Classification

The particle types are estimated using the fuzzy-logic polarimetric radar hydrometeor classification algorithm (Park et al., 2009). Several modifications were made to account for local features, such as adjusting membership function thresholds (Wu, Liu, et al., 2018) and applying environmental temperature thresholds. The algorithm classifies eight hydrometeor types: dry aggregated snow, wet snow, crystals of various orientations, graupel, big drops, light and moderate rain, heavy rain, and a mixture of rain and hail. These classifications provide insights into the underlying microphysical processes. The big drop category designates rain with the RSD skewed toward large drops, typically resulting from size sorting associated with convective updrafts or wind shear and veering. The graupel and the mixture of rain and hail categories imply riming processes. Notably, this algorithm cannot quantify the amount of hydrometeors and is limited to identifying one dominant type of hydrometeor in regions where multiple types coexist.

2.4. Estimation of the IWC

IWC is estimated using the method outlined by Ryzhkov et al. (2018), where the IWC is retrieved from K_{DP} and Z_{dr}:

Table 1
Details of the Frontal Rainfall and WR Events

FR		WR	
Dates	Synopsis	Dates	Synopsis
23–24 June 2019	Shear line	26–27 May 2019	Southerly wind speed convergence
11 May 2020	Front	29–30 May 2019	Monsoon trough
21–22 May 2020	Low vortex	24–25 May 2020	Monsoon trough
25–26 May 2020	Front	29–31 May 2020	Strong southwest monsoon
3 June 2021	Front	1–2 June 2020	Strong southwest monsoon
		6–8 June 2020	Strong southwest monsoon
		27–28 June 2021	Strong southwest monsoon

$$\mathrm{IWC} \approx 4.0 \times 10^{-3} \frac{K_{\mathrm{DP}}\lambda}{1 - Z_{\mathrm{dr}}^{-1}} \tag{7}$$

Here, λ is the radar wavelength expressed in mm and Z_{dr} is in the linear unit form of Z_{DR}. Ryzhkov et al. (2018) discussed the uncertainty of the IWC retrieval algorithm in detail. The retrieval results are affected by the degree of riming but are insensitive to the aspect ratios and orientations of ice particles. This method is thus more effective at lower temperatures, where riming is less likely. However, for some hydrometeors, such as heavily aggregated snow, the Z_{DR} and K_{DP} values can approach zero, which may lead to an underestimation of the IWC. To avoid large errors caused by low Z_{DR} values, we follow the approach of Wu et al. (2021) setting a minimum Z_{DR} value of 0.3 dB when $Z_{\mathrm{DR}} < 0.3$ dB.

3. Synoptic-Scale Environment and Convective Intensity

3.1. Synoptic Overview

Based on the type of mesoscale system forcing, the distance between front and rainstorm, and the extent of rain area, we select samples of FR and WR from the heavy rainfall events during the PRSC from 2019 to 2021. A total of five FR and seven WR events are selected (Table 1). Table 1 lists the synoptic-scale and mesoscale background systems associated with the heavy precipitation event, including mesoscale shear line, low vortex and front associated with FR events, and monsoon trough, strong southwest monsoon and monsoon flow convergence associated with WR events. These cases are highly representative, encompassing the majority of weather systems during the PRSC, although the sample size is relatively small.

Previous studies (Huang, 1986; Luo et al., 2020; Wu et al., 2020) have shown that the circulation patterns of FR and WR in South China region are significantly different. We produce composite synoptic patterns for the FR and WR events by averaging cover the cases of the same type using the ERA5 reanalysis data set, revealing distinct patterns (Figure 2). At 925 hPa, southerly winds bring warm moist air to Guangdong Province mostly south of 25° N, and the equivalent potential temperature in the study area (Figures 2a and 2b, gray dashed circles) exceeds 345 K in both scenarios. These create favorable thermodynamic conditions for heavy rainfall. For the FR events, cold air brought in by the northerly winds reaches the Nanling Mountains (See Figure 1 for location). This cold air then converges with the warm moist airflow from south and triggers convection at around 24° N. As a result, there are positive vertical velocities (Figure 2c, red contours) and precipitation in this region. In comparison, for WR events, the southerly winds extend further north to ~27° N before turning northwest. Cold air from the north usually has no direct contact in the region of warm sector rainfall. WR events are characterized by stronger southerly winds at the lower levels than FR events (Figures 2c and 2d) that often reach the intensity of boundary layer low-level jet (Du & Chen, 2018). Frictional deceleration by the land surface causes the southerly winds to converge near the coastline (Figure 2d) and the associated wind speed convergence produces mesoscale lifting that can initiate convection along the coast. Compared the WR events, the strong confrontation between the northerly and southerly winds results in a greater horizontal convergence in FR events, leading to stronger and more organized vertical motion (Figure 2c vs. Figure 2d, red contours).

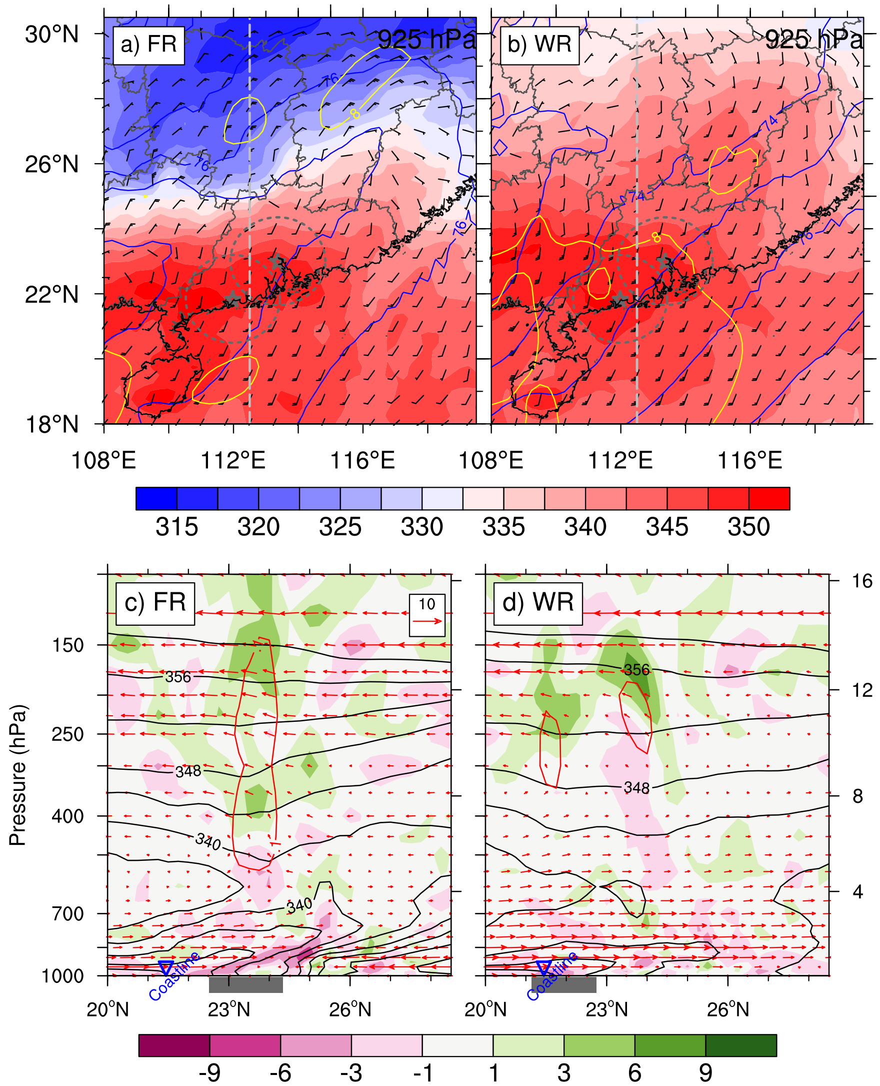

Figure 2. Composite synoptic background patterns for frontal rainfall (left panels) and WR (right panels) events. Equivalent potential temperature (shading; units: K), geopotential height (blue contours; units: 10 gpm), wind speeds >8 m s^{-1} (yellow contours), and wind fields (full bars, 4 m s^{-1}) at 925 hPa (upper panels). Height-latitude cross section of divergence (shading; units: 10^{-5} s^{-1}), equivalent potential temperature (black contours; units: K), 0.1 m s^{-1} vertical velocity contours (red contours), and wind vectors along 112.5° E (lower panels). The pentagrams and gray dashed circles (a, b) are the site locations and 150 km scanning range for GZ-POL and YJ-POL, respectively. The gray square in panels (c, d) marks the latitudinal position of precipitation and the blue triangle indicates the coastline location.

We select several vertical profiles in the upwind direction of each convective storm during the convection initiation stage and composite the soundings and wind hodographs for FR and WR (Figure 3). Both FR and WR have similar convective available potential energy (CAPE, of about 1500 J kg^{-1}), precipitable water vapor (PWV, about 70 mm), and convective inhibition energy (CIN, about 11 J kg^{-1}). These results indicate that the thermodynamic conditions for FR and WR are similar. However, their wind fields and corresponding dynamic conditions are significantly different. The magnitude of the 0–3 km storm relative helicity (SRH) for FR reaches about 128 m^2 s^{-2}, which is about 50% higher than that for WR. At the same time, FR shows stronger vertical wind shear with a value of ~13 m s^{-1} between 0 and 6 km height. Stronger wind shear enhances the tilt and longevity of convective updrafts, allowing supercooled liquid water to be transported to higher altitudes where it can contribute to more efficient ice-phase processes. Therefore, these parameters indicate that FR events have a greater potential to develop into deep convection.

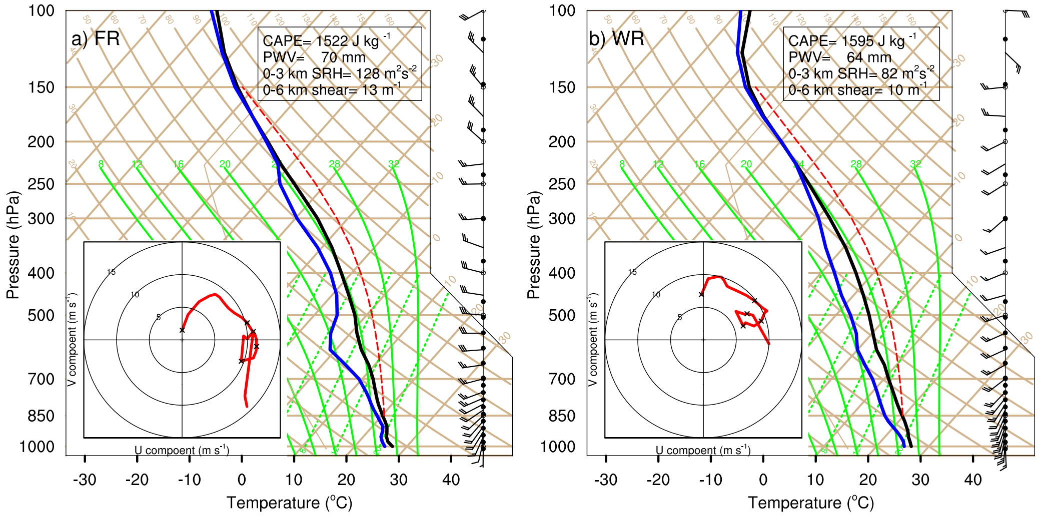

Figure 3. Composite skew *T* diagrams for (a) frontal rainfall and (b) WR. The insets are hodographs of the wind speed. The black crosses in the hodographs represent heights of 0.1, 3, 6, 9, and 12 km. Convective available potential energy, precipitable water vapor, storm relative helicity, and 0–6 km shear are given in the plots.

3.2. Convective Intensity

The present study focuses on the convective regions due to their predominant role in generating heavy rainfall. Convective cells (CCs) are identified by the method of Steiner et al. (1995). Six-min rain rates and lightning flash rates are then matched to the CCs.

Figure 4 presents statistical properties of CCs for FR and WR. FR has higher rain rates with a higher median value (Figure 4a). The mean and median values of the 50 dBZ echo-top height are larger for FR than for WR (Figure 4b) indicating stronger storm updrafts. The distributions of the lightning flash rates show a higher mean value of 0.93 for FR compared to 0.48 for WR (Figure 4c), further indicating stronger updrafts in FR. Previous studies (Carey & Rutledge, 2000; Deierling et al., 2008) also reported that stronger updrafts can transport more supercooled liquid water to higher altitudes, enhancing the riming process, which is an essential mechanism for graupel growth and lightning production.

4. Microphysical Characteristics of FR and WR

4.1. Microphysical Characteristics at 1.5 km Height

Figure 5 shows the joint probability density functions (PDFs) of Z_H and Z_{DR} at 1.5 km height for FR and WR CCs. Following the normalization procedure of Hence and Houze (2011), the PDFs are scaled by the maximum frequency, where 100% represents the most frequent joint value and values exceeding 50% define the modal distribution. For FR cases, the modal distribution spans Z_H values of 35–49 dBZ and Z_{DR} values of 0.4–1.2 dB. Notably, about 1.1% of the observations exceed 50 dBZ in Z_H and 2 dB in Z_{DR} (Figure 5a). The WR has a nearly identical Z_H distribution as FR (Figure 5b). However, WR has a slightly narrower modal distribution of Z_{DR} and fewer (0.6%) samples exceeding 50 dBZ for Z_H and 2 dB for Z_{DR}, suggesting that WR produces precipitation with smaller raindrop sizes than FR.

Figure 6 shows the joint PDFs of Z_H and K_{DP}. In the convective region, both FR and WR show a large slope in the relation between K_{DP} and Z_H, suggesting a rapid increase in K_{DP} when Z_H increases. FR exhibit higher frequencies (1.6%) of Z_H exceeding 50 dBZ and K_{DP} exceeding 2.0° km^{-1} than WR (0.8%), implying more abundant medium-sized raindrops. This is consistent with the higher PWV in soundings of FR (Figure 3).

To examine the size distribution characteristics of raindrops for the two types of CCs, we calculate joint PDFs of D_m and $\log_{10}(N_w)$ at 1.5 km altitude for FR and WR (Figure 7). The two gray rectangles in Figure 7 mark the parameter spaces for maritime-like and continental-like CCs as defined by Bringi et al. (2003). Both FR and WR are located around that of typical maritime-type convective precipitation where RSD is marked by a high

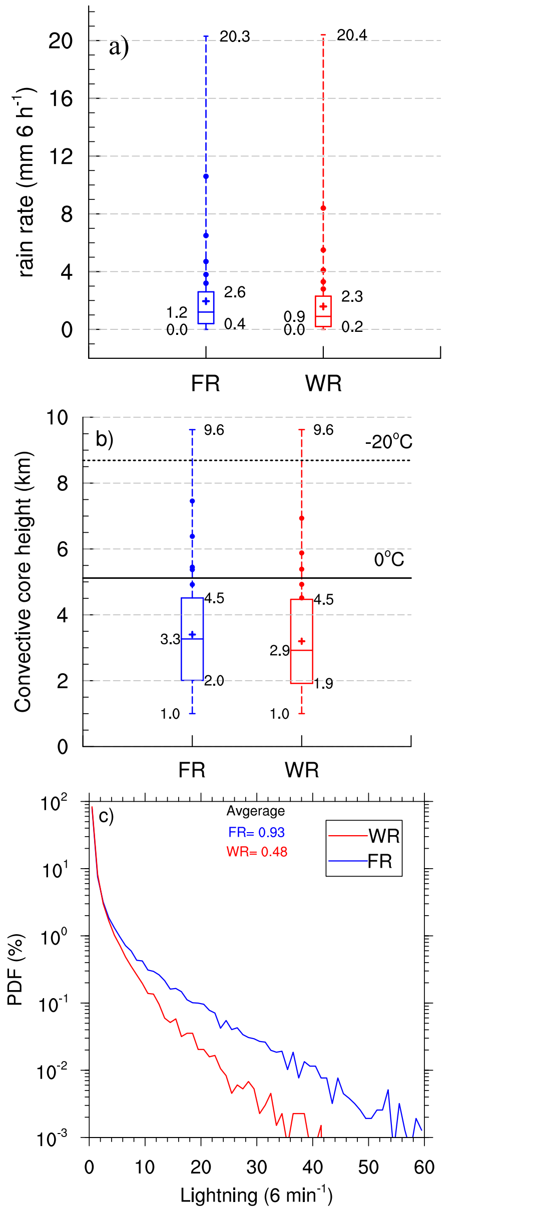

Figure 4. Box plots of (a) the 6-min rain rates and (b) the 50 dBZ echo-top heights for frontal rainfall (FR) and WR. The dots and crosses represent from bottom to top, the 80, 85, 90, 95, and 99 percentiles and the average values, respectively. The black lines in part (b) represent the levels of the −20 and 0°C environments, respectively. (c) Probability density function of the lightning flash rates for FR and WR.

concentration of small drops. Since both FR and WR occur in the coastal areas of South China during May–June with similar climatic background, water vapor content and aerosol concentrations. It is not surprising that they exhibit similar raindrop characteristics.

For WR, the number concentration is slightly higher, whereas the raindrop size is slightly smaller than that in FR. The mean values of D_m and $\log_{10}(N_w)$ for WR are 1.64 mm and 4.33, respectively, compared to 1.72 mm and 4.14 for FR. Meanwhile, there are fewer samples of WR in the continental-like cluster, indicating that the convective intensity is slightly weaker than that of FR. This finding aligns with the lightning statistics in Section 3.2.

Figure 7 also shows results from other study regions for comparison. Similar to our study, the $D_m - \log_{10}(N_w)$ pairs of convective rain over other regions—including Meiyu rainfall in East China (Wen et al., 2020), Baiu front rainfall in Japan (Oue et al., 2011), Changma rainfall over South Korea (Suh et al., 2016), and convective rain in Taiwan (Seela et al., 2017)—are also distributed near the maritime cluster. These regions share some common features: (a) they are all coastal regions, and (b) they are all closely related to the East Asia summer monsoon. As a result, the warm, moist oceanic flow exerts a strong influence on the precipitation systems leading to the maritime nature of the convective rain. For the two types of convective rain during the PRSC, Han et al. (2021) found based on a single case that both warm sector and frontal CCs were mainly within the maritime-like cluster in the statistics of a heavy rainfall event during the PRSC (their Figure 8) agreeing with our study. However, different from our case, CCs in the warm-sector had stronger intensity than those in the frontal region in their case. Unlike our study, their case demonstrated that the WR had more favorable environmental conditions for convective development specifically a higher CAPE.

4.2. Comparison of the Vertical Structures

Figure 8 shows vertical percentile profiles of Z_H, Z_{DR}, and K_{DP} in the frontal and warm sector CCs. Below the melting layer, the Z_H values for both FR and WR are nearly identical and remain relatively constant with height. However, their differences become apparent above the melting layer (Figure 8a). Previous studies (Han et al., 2021; Xu et al., 2009) have demonstrated that the vertical profile of radar reflectivity can serve as an indicator of storm intensity. The larger vertical profiles of Z_H at the 90th and 99th percentiles indicate that FR generally has stronger convection intensity than WR. In particular, ice-phase microphysical processes (e.g., aggregation and riming) of FR are more active between 6 and 10 km than those of WR.

The differences between FR and WR are more visible for Z_{DR} and K_{DP} than for Z_H. From the 50th to 90th percentile, the Z_{DR} differences increase from 0.15 to 0.25 dB, whereas the K_{DP} differences are more pronounced, increasing from about 0.0 to 0.35° km^{-1} below the melting layer. Together, these results imply that the FR has larger sized particles caused by stronger convection. Additionally, as convective intensity increases, the differences in the microphysical processes between FR and WR become more pronounced, although further evidence is required to fully reveal the underlying microphysical mechanisms.

The characteristics of the polarimetric profiles show that particle growth processes above the 0°C level could be divided into two layers. In the upper layer (7–12 km), Z_H increases while Z_{DR} decreases, indicating that the dominant process is aggregation. In the lower layer (7 km to the 5 km), three polarimetric variables (Z_H, Z_{DR}, and K_{DP}) show a sharp increase, suggesting active riming. These microphysical processes and their corresponding polarimetric variable profiles have been documented in other observational studies (Kumjian, 2013; Wu, Zhao, et al., 2018).

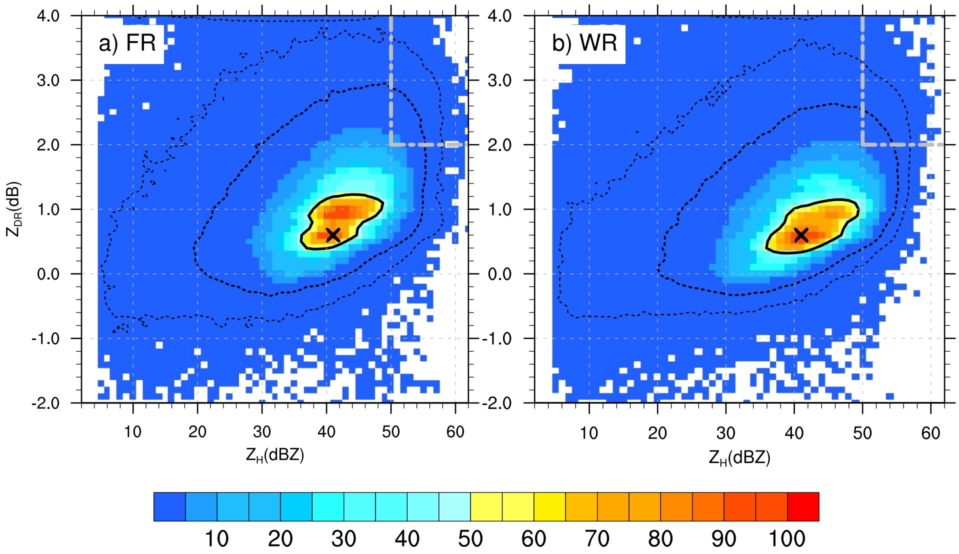

Figure 5. Joint frequency distributions of Z_H (dBZ) and Z_{DR} (dB) at 1.5 km height for (a) frontal rainfall and (b) WR normalized by the maximum frequency in the data set. The black contours indicate percentages of 0.1%, 1% (dashed lines), and 50% (solid lines). The maximum frequency is marked by the crosses.

4.3. Ice Microphysical Processes

Figure 9 compares the vertical distributions of hydrometeors for FR and WR. The frequency difference in the hydrometeors mainly occurs below 9 km height (the −20°C level). The riming process, where supercooled liquid water collides and accretes onto ice particles, is active between the −12 and 0°C levels (Kneifel & Moisseev, 2020).

The frontal CCs have more ice crystals and less dry snow between 7 and 10 km height. Meanwhile, the larger Z_{DR} values (Figure 8b) and longer melting path (Figure 9) imply larger sizes of graupel in FR, which is associated with stronger convection. The synthesis results for the ERA5 reanalysis data set show that the FR and WR have a similar total column vertically integrated water vapor, but the supercooled liquid water content of FR is three times that of WR (Figure 10). We speculate that this difference arises because the stronger updrafts in FR bring more water vapor to the supercooled region, thereby enhancing riming—a key process in graupel formation.

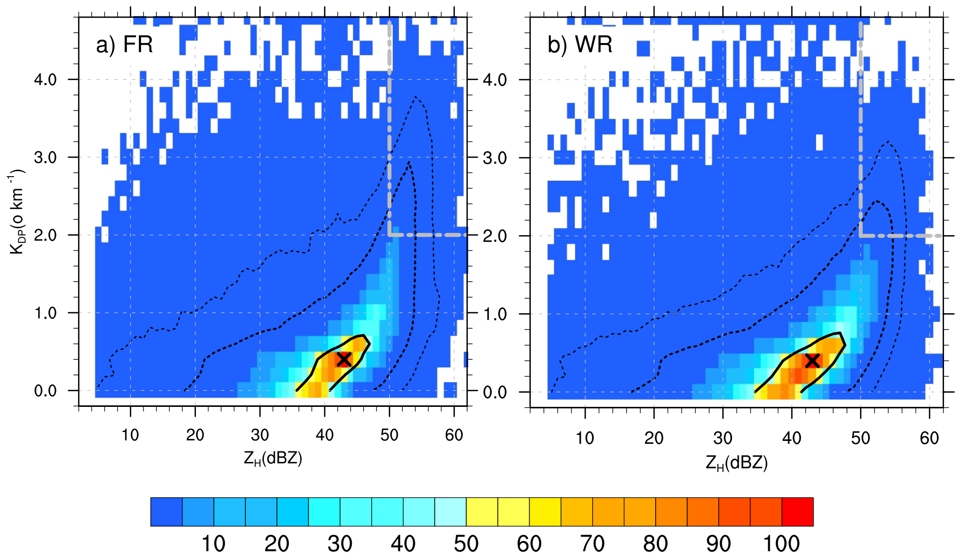

Figure 6. Same as Figure 5 but for but for the joint frequency distributions of Z_H (dBZ) and K_{DP} (° km^{-1}) at 1.5 km height.

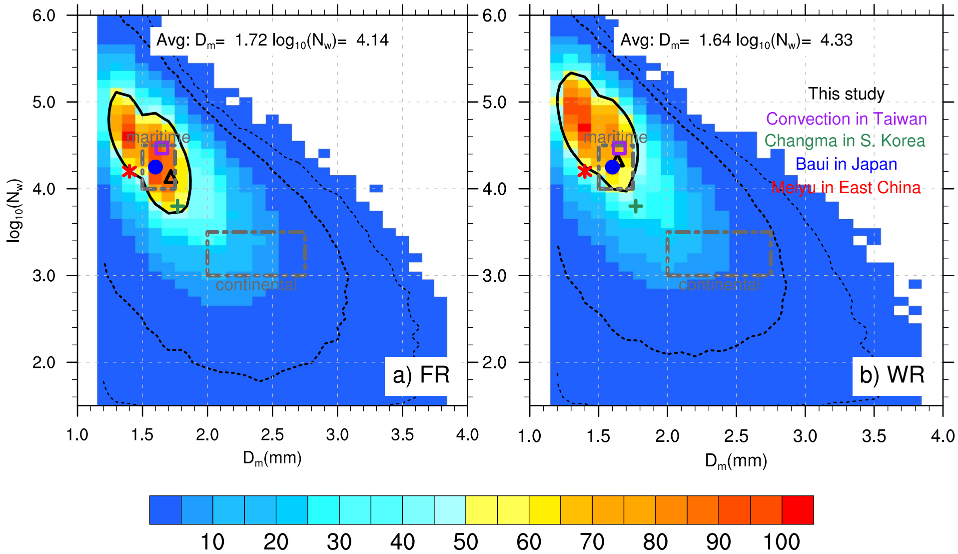

Figure 7. Same as Figure 5, but for but for the joint frequency distributions of D_m (mm) and $\log_{10}(N_w)$ ($mm^{-1}\ m^{-3}$). The two gray dashed rectangles represent the maritime and continental types of convective precipitation reported by Bringi et al. (2003) while the means from several other studies are also marked in the figure.

Below the melting layer, big raindrops occur with a frequency of about 1.1% at 1.5 km height in FR compared to only 0.6% in WR. This suggests the melting of more graupel particles in FR. However, the mixture of rain and hail is almost negligible in the frequency statistics due to insufficient convection in both FR and WR events.

4.4. Warm Rain Microphysical Processes

To better understand the microphysical processes and their vertical variations in heavy rainfall over PRSC, Figure 11 compares the radar-retrieved profiles of D_m at the 50th, 90th, and 99th percentiles and the corresponding $\log_{10}N_w$ profiles for FR and WR CCs. The frontal CCs have larger D_m and smaller $\log_{10}N_w$ values than the warm sector CCs at all altitudes consistent with the larger Z_{DR} values below the melting layer in FR. The D_m ($\log_{10}N_w$) slightly increases (decreases) from 4.5 to 1.4 km height, suggesting that the growth of raindrops during descent should be collision, coalescence, and collection of the raindrops and cloud droplets. These features are consistent with the simultaneous increase in Z_H, Z_{DR}, and K_{DP} (Figure 8). Consistent with previous studies (Wang et al., 2023; Yu et al., 2022), these warm rain processes play a crucial role in the raindrop growth and the production of heavy rainfall during PRSC. At the 90th and 99th percentiles, the D_m values in FR decrease from 1.4 to

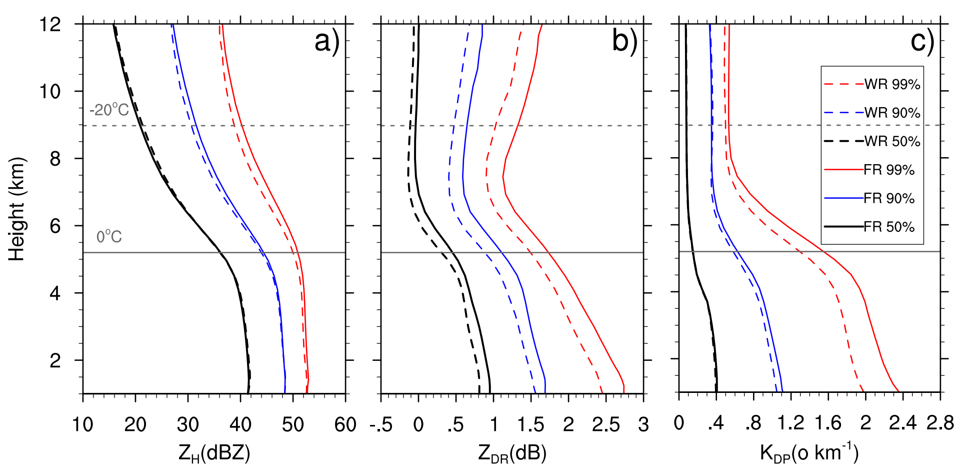

Figure 8. Vertical profiles of (a) Z_H, (b) Z_{DR}, and (c) K_{DP} at 50, 90, and 99 percentiles for frontal rainfall (solid lines) and WR (dashed lines). The horizontal lines indicate −20°C (dashed) and 0°C (solid) temperature levels of the environment.

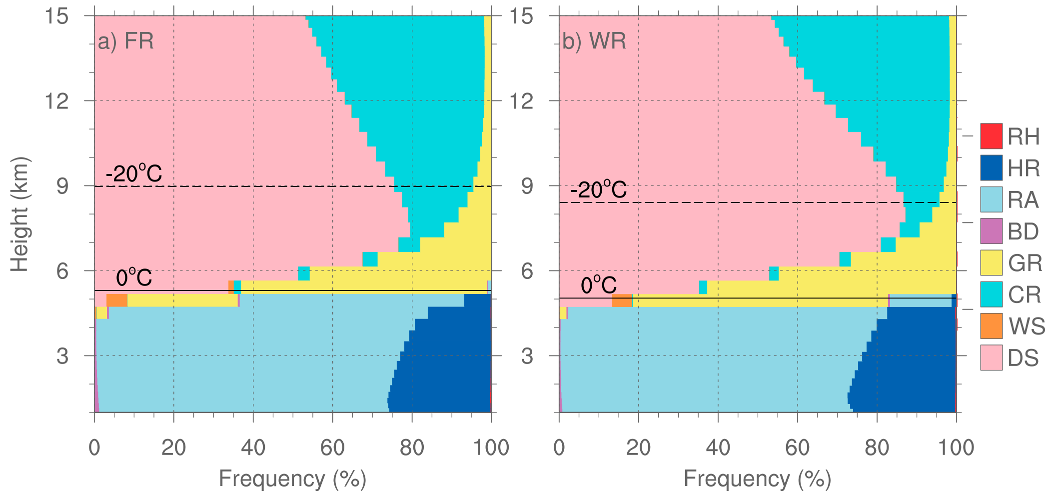

Figure 9. Stacked frequency (%) of hydrometeors at different altitudes for (a) frontal rainfall and (b) WR. The hydrometeor types are: DS for dry aggregated snow, WS for wet snow, CR for crystals of various orientations, GR for graupel, BD for big raindrops, RA for light and moderate rain, HR for heavy rain, and RH for the mixture of rain and hail. The black horizontal lines (from top to bottom) represent the −20 and 0°C isotherms.

0.6 km. This is probably a result of the breakup of oversized raindrops in frontal CCs. Additionally, raindrop evaporation also contributes to the reduction of D_m to some extent (Hu & Srivastava, 1995).

To estimate the relative importance of warm-rain versus ice-phase processes in producing heavy rainfall, we compare the vertical profiles of retrieved LWC and IWC (Figure 12). The LWC exhibits magnitudes approximately two to three times those of IWC with 99th percentile maxima of 17.4 and 4.8 g m^{-3}, respectively. Even under the assumption of complete melting of ice-phase particles above the freezing level, their contributions would only account for about 28% of the liquid water near the surface. This suggests that warm rain processes are the primary contributors to precipitation formation in both frontal and warm sector CCs.

The ratio of IWC to LWC shows a similar pattern to previous studies over South China (Han et al., 2021; Huang et al., 2023), typhoon rainbands (Wang et al., 2016; Wu, Zhao, et al., 2018), and subtropical squall line in East China (Wen et al., 2017). In addition, the median ratio of IWC to LWC is about 0.38 in FR and 0.32 in WR, indicating that ice-phase microphysical processes contribute more significantly to precipitation in FR than in WR. The 99th percentile IWC for FR between 5.5 and 8 km height is slightly larger than that for WR, implying that the extreme frontal CCs have more active ice-phase processes. This characteristic corresponds to the increased amount of large-sized graupel in FR (Figure 9). Since WR events occur near the coastline and are closer to the

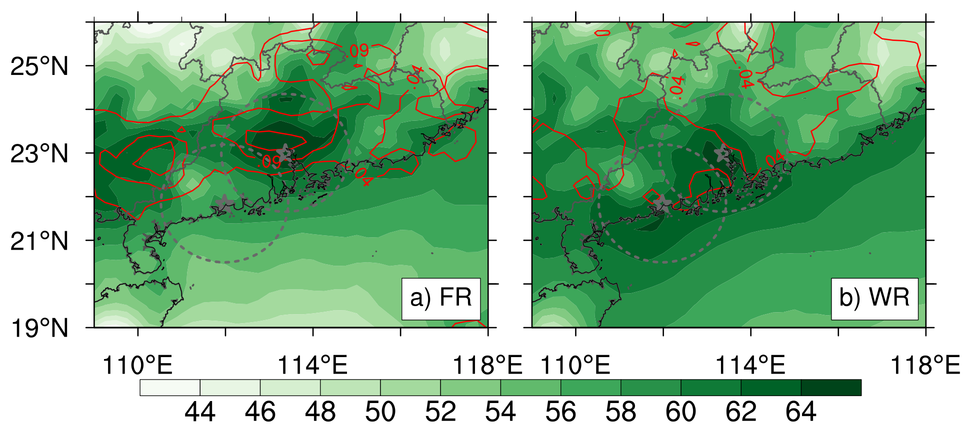

Figure 10. Total column vertically integrated water vapor (shading; units: kg m^{-2}) and supercooled liquid water (contours starting at 0.04 kg m^{-2} with intervals of 0.05 kg m^{-2}) composited from the ERA5 reanalysis data set for (a) frontal rainfall and (b) WR.

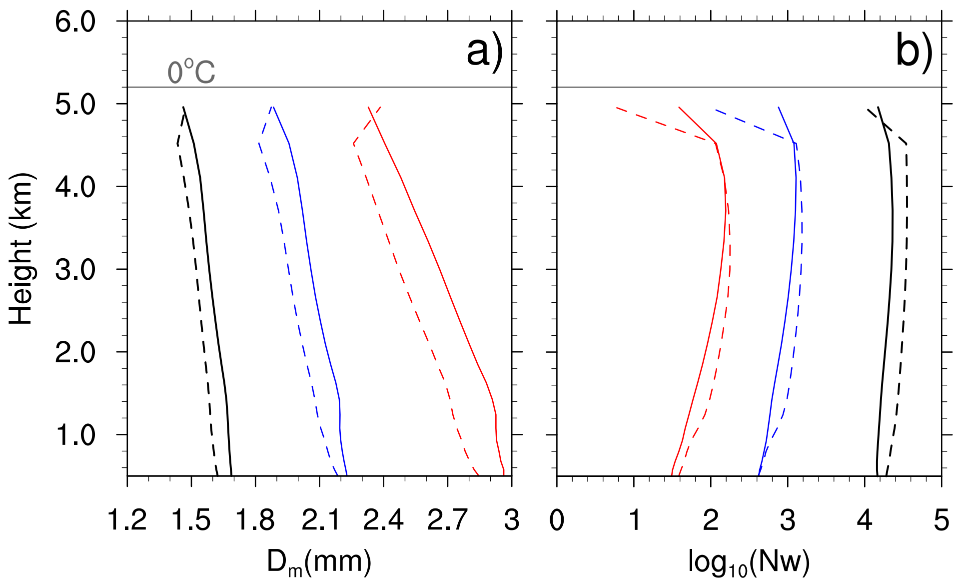

Figure 11. Vertical profiles of (a) D_m at the 50th (black), 90th (blue), and 99th (red) percentiles and (b) the corresponding $\log_{10}N_w$ profiles for frontal rainfall (solid lines) and WR (dashed lines). The horizontal line represents the level of 0°C isotherm.

moisture source, they exhibit higher LWC. This suggests that warm sector CCs may produce more medium-sized raindrops through collision-coalescence processes and/or the collection of cloud water by raindrops.

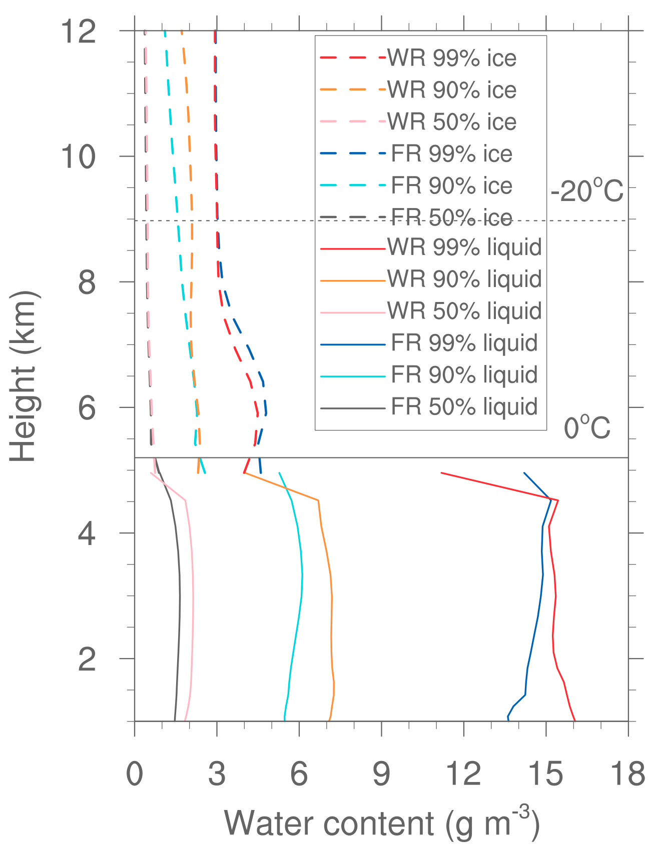

Figure 12. Same as Figure 8, but for liquid (solid lines) and ice (dashed lines) water content.

Based on the above analyses, a conceptual model of environmental factors and microphysical features of PRSC FR and WR is proposed and presented in Figure 13. In FR, northerly cold air converges with southerly monsoon airflow near 24° N during PRSC, resulting in the development of strong convection over the windward mountains of Nanling. In contrast, WR primarily occurs within the southerly warm humid monsoon airflow. Under strong southerly flows, sometime in the form of boundary layer low-level jet, frictional deceleration caused by the rougher land surface can produce wind speed convergence near the coastline (Chen et al., 2014), serving as the main triggering and forcing mechanism of warm sector CCs (Figure 13b). In some other cases, the wind speed convergence at the terminus of the boundary layer jet can provide similar triggering effect (Du et al., 2022). As the moisture is consumed by coastal rainfall, less or little rain is produced further north on the windward mountain slopes, unless there is significant frontal or other mesoscale forcing. The circulation patterns of FR and WR presented here are consistent with the 12-year statistical results of Wu et al. (2020). The FR and WR have comparable thermodynamic conditions, but FR benefits from the more favorable dynamic conditions specifically the higher 0–3 km SRH and stronger 0–6 km wind shear. These dynamic conditions support stronger updrafts than in WR, leading to higher core convection height and more active ice-phase processes (e.g., riming); consequently, larger graupels form in the riming zone of FR. The melting of these larger graupels produce more large-sized raindrops below the melting layer in FR compared to WR. Despite these differences, collision-coalescence is the dominant growth process of raindrops in both FR and WR.

5. Summary and Discussion

In this study, we investigated two types of heavy rainfall events during the pre-summer rainfall PRSC from 2019 to 2021. The first type includes events

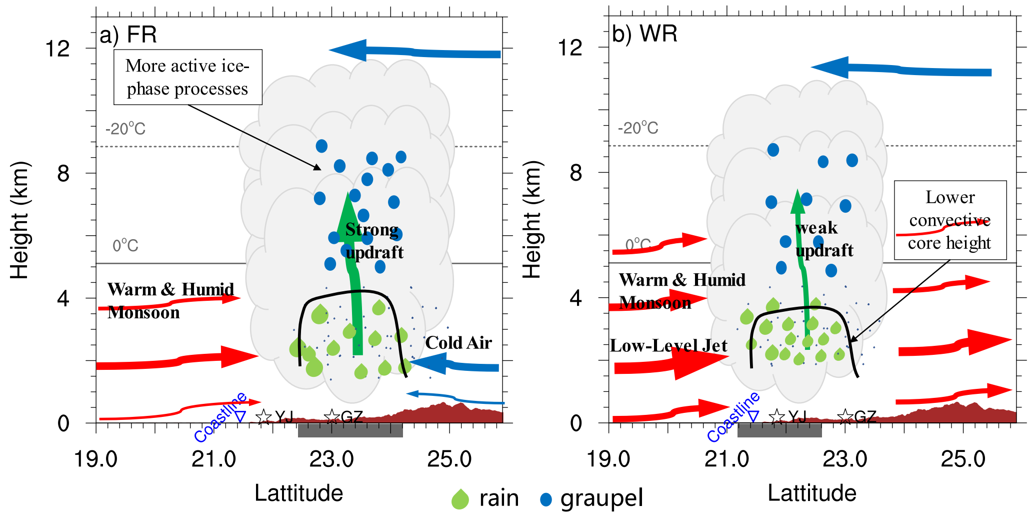

Figure 13. Schematic diagrams of the environmental wind fields and microphysical processes for (a) strongly forced frontal type rain (frontal rainfall (FR)) and (b) weakly forced warm sector rain (WR). The gray thick line at the bottom indicates the latitudinal zone of precipitation. The red, blue, and green arrows indicate southerly, northerly, and updraft flows, respectively. The thickness of the arrows represents the wind speed. FR occurs at the convergence zone of the northerly and southerly flows at the front or other form of mesoscale convergence, whereas WR occurs in the speed convergence zone of southerly flows near the coastline or at the terminus of a low-level jet. The thick black link represents the 50 dBZ echo boundary. Stronger convergence leads to stronger upward motion in FR, resulting in a somewhat deeper convective core than that of WR. Thus, FR has more active ice phase processes, producing more graupel that melts into large-sized raindrops below the melting level.

associated with well-defined synoptic-scale or mesoscale systems, such as front, shear line, and low vortex with strong forcing, and for simplicity, this type is referred to as FR. The second type consists of events that occur in prevailing southerly monsoon flows typically in the warm sector away from a front or other types of mesoscale systems, and this type is denoted as warm sector rainfall (WR). We analyzed their microphysical characteristics and processes using S-band polarimetric radar observations from Guangzhou and Yangjiang, AWS measurements, lightning detection data, and the ERA5 reanalysis data set.

FR CCs develop in strongly forced environments near mesoscale systems benefiting from the associated dynamic lifting. In contrast, WR CCs are mostly initiated near the coastline, influenced by the convergence of southerly flow, either due to deceleration by land surface friction or wind speed convergence at the terminus of the boundary layer low-level jet (Luo et al., 2020; Wu et al., 2020). Despite their different forcing mechanisms, FR and WR experience similar thermodynamic conditions, including CAPE, convective inhibition, and vertically integrated PWV. However, FR events feature more favorable dynamic environmental parameters, such as the storm-relative helicity and bulk wind shear that promote the development of deep convection. This is reflected in the higher echo-tops and higher lightning flash rates of the FR events.

Both FR and WR CCs exhibit maritime type raindrop distributions, as they form in the same climatic region with comparable water vapor and aerosol contents. This finding is consistent with observational studies from other coastal regions in East Asian monsoon region (Oue et al., 2011; Suh et al., 2016; Wen et al., 2020; Yu et al., 2022). FR events are characterized by slightly larger raindrop mean diameter D_m and smaller raindrop total number concentration N_w, leading to higher differential reflectivity (Z_{DR}) measurements. Vertical profiles of polarimetric radar variables suggest that FR has stronger convection especially more active riming process between the 0 and −20°C levels. Consequently, larger graupel particles and an increased presence of large raindrops are observed supported by the hydrometeor classification (Park et al., 2009) and the supercooled liquid water distributions.

Both FR and WR experience an increase in D_m and slight decrease in N_w with height, suggesting the warm rain processes—especially the collision and coalescence of cloud water by raindrops— play a dominant role in raindrops growth (Wang et al., 2023; Yu et al., 2022). A decrease in D_m below 1.4 km height is present in some frontal CCs likely due to the breakup and evaporation of oversized raindrops. This decrease is absent in warm sector CCs. The ratio of IWC to LWC, approximately 0.38 in FR and 0.32 in WR, further supports the dominance of warm rain processes in both event types. However, the greater contribution of melting ice-phase particles in FR suggests a more significant role of ice-phase processes compared to WR.

The results presented in this study enhance our understanding of the microphysical characteristics of heavy rainfall in the tropical monsoon region of Southern China, where precipitation forecasting remains a challenge. However, the formation mechanisms of heavy precipitation, in particular in the warm sector, are still not completely understood. Due to the limited accuracy of observed and retrieved microphysical variables (Huang et al., 2019), the statistical results derived from observations may not fully capture all underlying microphysical processes. Future research should employ cloud-resolving numerical simulations to further investigate these processes and assess their relative importance. Additionally, localized factors such as localized land-sea effects (e.g., Chen et al., 2016), the effects of urban regions (e.g., Lin et al., 2021) and the effects of anthropogenic aerosols (e.g., Guo et al., 2022) should be considered in future studies to refine our understanding of heavy rainfall dynamics in this region.

Data Availability Statement

Measurements used in this study, including S-band polarimetric radar, lightning detection, and surface AWSs, are obtained from the China Meteorological Administration. Although the original observations are not publicly accessible online, the derived secondary data products utilized used in this study are accessible via Harvard Dataverse (Wang, 2024). Additionally, the fifth-generation European Centre for Medium-Range Weather Forecasts reanalysis data (ERA5; Hersbach et al. (2018)) are employed available at https://cds.climate.copernicus.eu/. Figures are made with the NCAR Command Language (Version 6.6.2) [Software] (2019) available at https://www.ncl.ucar.edu/. The corresponding scripts are also archived at the Harvard Dataverse (Wang, 2024).

Acknowledgments
This study was supported by the National Key R&D Program of China Grant 2023YFC3008001, the National Natural Science Foundation of China Grant 41730965 and the Youth Innovation Team of China Meteorological Administration (CMA2023QN07 and CMA2024QN01).

References

Bringi, V. N., Chandrasekar, V., Hubbert, J., Gorgucci, E., Randeu, W. L., & Schoenhuber, M. (2003). Raindrop size distribution in different climatic regimes from disdrometer and dual-polarized radar analysis. *Journal of the Atmospheric Sciences*, *60*(2), 354–365. https://doi.org/10.1175/1520-0469(2003)060<0354:RSDIDC>2.0.CO;2

Cao, Q., Zhang, G., & Xue, M. (2013). A variational approach for retrieving raindrop size distribution from polarimetric radar measurements in the presence of attenuation. *Journal of Applied Meteorology and Climatology*, *52*(1), 169–185. https://doi.org/10.1175/jamc-d-12-0101.1

Carey, L. D., & Rutledge, S. A. (2000). The relationship between precipitation and lightning in tropical island convection: A C-band polarimetric radar study. *Monthly Weather Review*, *128*(8), 2687–2710. https://doi.org/10.1175/1520-0493(2000)128<2687:TRBPAL>2.0.CO;2

Chen, G., Zhao, K., Wen, L., Wang, M., Huang, H., Wang, M., et al. (2019). Microphysical characteristics of three convective events with intense rainfall observed by polarimetric radar and disdrometer in Eastern China. *Remote Sensing*, *11*(17), 2004. https://doi.org/10.3390/rs11172004

Chen, X., Zhang, F., & Zhao, K. (2016). Diurnal variations of the land–sea breeze and its related precipitation over South China. *Journal of the Atmospheric Sciences*, *73*(12), 4793–4815. https://doi.org/10.1175/JAS-D-16-0106.1

Chen, X., Zhao, K., & Xue, M. (2014). Spatial and temporal characteristics of warm season convection over Pearl River Delta region, China, based on 3 years of operational radar data. *Journal of Geophysical Research: Atmospheres*, *119*(22), 12447–412465. https://doi.org/10.1002/2014JD021965

Deierling, W., Petersen, W. A., Latham, J., Ellis, S., & Christian, H. J. (2008). The relationship between lightning activity and ice fluxes in thunderstorms. *Journal of Geophysical Research*, *113*(D15). https://doi.org/10.1029/2007JD009700

Ding, Y., Li, C., & Liu, Y. (2004). Overview of the South China sea monsoon experiment. *Advances in Atmospheric Sciences*, *21*(3), 343–360. https://doi.org/10.1007/BF02915563

Du, Y., & Chen, G. (2018). Heavy rainfall associated with double low-level jets over southern China. Part I: Ensemble-based analysis. *Monthly Weather Review*, *146*(11), 3827–3844. https://doi.org/10.1175/MWR-D-18-0101.1

Du, Y., Shen, Y., & Chen, G. (2022). Influence of coastal marine boundary layer jets on rainfall in South China. *Advances in Atmospheric Sciences*, *39*(5), 782–801. https://doi.org/10.1007/s00376-021-1195-7

Guo, J., Luo, Y., Yang, J., Furtado, K., & Lei, H. (2022). Effects of anthropogenic and sea salt aerosols on a heavy rainfall event during the early-summer rainy season over coastal Southern China. *Atmospheric Research*, *265*(105923), 1–15. https://doi.org/10.1016/j.atmosres.2021.105923

Han, B., Du, Y., Wu, C., & Liu, X. (2021). Microphysical characteristics of the coexisting frontal and warm-sector heavy rainfall in South China. *Journal of Geophysical Research: Atmospheres*, *126*(21), e2021JD035446. https://doi.org/10.1029/2021JD035446

Hence, D. A., & Houze, R. A., Jr. (2011). Vertical structure of hurricane eyewalls as seen by the TRMM precipitation radar. *Journal of the Atmospheric Sciences*, *68*(8), 1637–1652. https://doi.org/10.1175/2011JAS3578.1

Hersbach, H., Bell, B., Berrisford, P., Biavati, G., Horányi, A., Muñoz Sabater, J., et al. (2018). ERA5 hourly data on pressure levels from 1979 to present. Retrieved from https://cds.climate.copernicus.eu/

Hu, Z., & Srivastava, R. C. (1995). Evolution of raindrop size distribution by coalescence, breakup, and evaporation: Theory. *Journal of the Atmospheric Sciences*, *52*(10), 1761–1783. https://doi.org/10.1175/1520-0469(1995)052<1761:EORSDB>2.0.CO;2

Huang, H., Zhang, G., Zhao, K., Liu, S., Wen, L., Chen, G., & Yang, Z. (2019). Uncertainty in retrieving raindrop size distribution from polarimetric radar measurements. *Journal of Atmospheric and Oceanic Technology*, *36*(4), 585–605. https://doi.org/10.1175/jtech-d-18-0107.1

Huang, H., Zhao, K., Chan, J. C. L., & Hu, D. (2023). Microphysical characteristics of extreme-rainfall convection over the Pearl River Delta region, South China from polarimetric radar data during the pre-summer rainy season. *Advances in Atmospheric Sciences*, *40*(5), 874–886. https://doi.org/10.1007/s00376-022-1319-8

Huang, S. S. (1986). *Heavy rainfall over southern China in the pre-summer rainy season (in Chinese)*. Guangdong Science and Technology Press. P244.

Jiang, H., Yang, Y., Bai, Y., & Wang, H. (2019). Evaluation of the total, direct, and diffuse solar radiations from the ERA5 reanalysis data in China. *IEEE Geoscience and Remote Sensing Letters*, *17*(1), 47–51. https://doi.org/10.1109/LGRS.2019.2916410

Kneifel, S., & Moisseev, D. (2020). Long-term statistics of riming in nonconvective clouds derived from ground-based Doppler cloud radar observations. *Journal of the Atmospheric Sciences*, *77*(10), 3495–3508. https://doi.org/10.1175/jas-d-20-0007.1

Kretzschmar, J., Stapf, J., Klocke, D., Wendisch, M., & Quaas, J. (2020). Employing airborne radiation and cloud microphysics observations to improve cloud representation in ICON at kilometer-scale resolution in the Arctic. *Atmospheric Chemistry and Physics*, *20*(21), 13145–13165. https://doi.org/10.5194/acp-20-13145-2020

Kumjian, M. R. (2013). Principles and applications of dual-polarization weather radar. Part I: Description of the polarimetric radar variables. *Journal of Operational Meteorology*, *1*(19), 226–242. https://doi.org/10.15191/nwajom.2013.0119

Lin, Y., Fan, J., Jeong, J.-H., Zhang, Y., Homeyer, C. R., & Wang, J. (2021). Urbanization-induced land and aerosol impacts on storm propagation and hail characteristics. *Journal of the Atmospheric Sciences*, *78*(3), 925–947. https://doi.org/10.1175/JAS-D-20-0106.1

Liu, R., Sun, J., & Chen, B. (2019). Selection and classification of warm-sector heavy rainfall events over South China. *Chinese Journal of Atmospheric Sciences*, *43*(1), 119–130. (in Chinese with an English abstract). https://doi.org/10.3878/j.issn.1006-9895.1803.17245

Liu, X., Luo, Y., Guan, Z., & Zhang, D.-L. (2018). An extreme rainfall event in coastal South China during scmrex-2014: Formation and roles of rainband and echo trainings. *Journal of Geophysical Research: Atmospheres*, *123*(17), 9256–9278. https://doi.org/10.1029/2018jd028418

Liu, X., Luo, Y., Huang, L., Zhang, D.-L., & Guan, Z. (2020). Roles of double low-level jets in the generation of coexisting inland and coastal heavy rainfall over South China during the presummer rainy season. *Journal of Geophysical Research: Atmospheres*, *125*(18), e2020JD032890. https://doi.org/10.1029/2020JD032890

Luo, Y., Xia, R., & Chan, J. C. L. (2020). Characteristics, physical mechanisms, and prediction of pre-summer rainfall over South China: Research progress during 2008-2019. *Journal of the Meteorological Society of Japan. Ser. II*, *98*(1), 19–42. https://doi.org/10.2151/jmsj.2020-002

Luo, Y., Zhang, R., Wan, Q., Wang, B., Wong, W. K., Hu, Z., et al. (2017). The Southern China monsoon rainfall experiment (SCMREX). *Bulletin of the American Meteorological Society*, *98*(5), 999–1013. https://doi.org/10.1175/BAMS-D-15-00235.1

NCAR Command Language. (2019). 753 UCAR/NCAR/CISL/TDD (Version 6.6.2) [software]. https://doi.org/10.5065/D6WD3XH5

Oue, M., Uyeda, H., & Lee, D.-I. (2011). Raindrop size distribution parameters estimated from polarimetric radar variables in convective cells around Okinawa island during the Baiu period. *Asia-Pacific Journal of Atmospheric Sciences*, *47*(1), 33–44. https://doi.org/10.1007/s13143-011-1003-x

Park, H., Ryzhkov, A. V., Zrnić, D. S., & Kim, K. E. (2009). The hydrometeor classification algorithm for the polarimetric WSR-88D: Description and application to an MCS. *Weather and Forecasting*, *24*(3), 730–748. https://doi.org/10.1175/2008WAF2222205.1

Ryzhkov, A. V., Bukovcic, P., Murphy, A., Zhang, P., & McFarquhar, G. (2018). Ice microphysical retrievals using polarimetric radar data. In *10th European Conference on Radar in Meteorology and Hydrology* (pp. 1–11).

Ryzhkov, A. V., Giangrande, S. E., & Schuur, T. J. (2005). Rainfall estimation with a polarimetric prototype of WSR-88D. *Journal of Applied Meteorology*, *44*(4), 502–515. https://doi.org/10.1175/jam2213.1

Ryzhkov, A. V., & Zrnic, D. S. (2019). Polarimetric "fingerprints" of different microphysical processes in clouds and precipitation In *Radar polarimetry for weather observations* (pp. 207–268). Springer International Publishing.

Seela, B. K., Janapati, J., Lin, P.-L., Reddy, K. K., Shirooka, R., & Wang, P. K. (2017). A comparison study of summer season raindrop size distribution between Palau and Taiwan, two islands in Western Pacific. *Journal of Geophysical Research: Atmospheres*, *122*(21), 11787–711805. https://doi.org/10.1002/2017JD026816

Steiner, M., Houze, R. A., & Yuter, S. E. (1995). Climatological characterization of three-dimensional storm structure from operational radar and rain gauge data. *Journal of Applied Meteorology and Climatology*, *34*(9), 1978–2007. https://doi.org/10.1175/1520-0450(1995)034<1978:Ccotds>2.0.Co;2

Suh, S. H., You, C. H., & Lee, D. I. (2016). Climatological characteristics of raindrop size distributions in Busan, Republic of Korea. *Hydrology and Earth System Sciences*, *20*(1), 193–207. https://doi.org/10.5194/hess-20-193-2016

Wang, H. (2024). Replication data for JGR: Atmospheres [Dataset]. https://doi.org/10.7910/DVN/FNVZEI

Wang, H., Kong, F., Jung, Y., Wu, N., & Yin, J. (2018). Quality control of S-band polarimetric radar measurements for data assimilation. *Journal of Applied Meteorological Science*, *29*(5), 546–558. (in Chinese with an English abstract). https://doi.org/10.11898/1001-7313.20180504

Wang, H., Kong, F., Wu, N., Lan, H., & Yin, J. (2019). An investigation into microphysical structure of a squall line in South China observed with a polarimetric radar and a disdrometer. *Atmospheric Research*, *226*(2), 171–180. https://doi.org/10.1016/j.atmosres.2019.04.009

Wang, H., Yin, J., Wu, N., & Ding, W. (2023). Microphysical structures of an extreme rainfall event over the coastal metropolitan city of Guangzhou, China: Observation analysis with polarimetric radar. *Asia-Pacific Journal of Atmospheric Sciences*, *59*(1), 3–16. https://doi.org/10.1007/s13143-022-00289-y

Wang, M., Zhao, K., Xue, M., Zhang, G., Liu, S., Wen, L., & Chen, G. (2016). Precipitation microphysics characteristics of a typhoon Matmo (2014) rainband after landfall over Eastern China based on polarimetric radar observations: Microphysics of typhoon rainband. *Journal of Geophysical Research: Atmospheres*, *121*(20), 12415–12433. https://doi.org/10.1002/2016JD025307

Wen, J., Zhao, K., Huang, H., Zhou, B., Yang, Z., Chen, G., et al. (2017). Evolution of microphysical structure of a subtropical squall line observed by a polarimetric radar and a disdrometer during OPACC in Eastern China. *Journal of Geophysical Research: Atmospheres*, *122*(15), 8033–8050. https://doi.org/10.1002/2016JD026346

Wen, L., Zhao, K., Yang, Z., Chen, H., Huang, H., Chen, G., & Yang, Z. (2020). Microphysics of stratiform and convective precipitation during Meiyu season in Eastern China. *Journal of Geophysical Research: Atmospheres*, *125*(24), e2020JD032677. https://doi.org/10.1029/2020JD032677

Wu, C., Liu, L., Wei, M., Xi, B., & Yu, M. (2018). Statistics-based optimization of the polarimetric radar hydrometeor classification algorithm and its application for a squall line in South China. *Advances in Atmospheric Sciences*, *35*(3), 296–316. https://doi.org/10.1007/s00376-017-6241-0

Wu, D., Zhang, F., Chen, X., Ryzhkov, A., Zhao, K., Kumjian, M. R., et al. (2021). Evaluation of microphysics schemes in tropical cyclones using polarimetric radar observations: Convective precipitation in an outer rainband. *Monthly Weather Review*, *149*(4), 1055–1068. https://doi.org/10.1175/MWR-D-19-0378.1

Wu, D., Zhao, K., Kumjian, M. R., Chen, X., Huang, H., Wang, M., et al. (2018). Kinematics and microphysics of convection in the outer rainband of typhoon Nida (2016) revealed by polarimetric radar. *Monthly Weather Review*, *146*(7), 2147–2159. https://doi.org/10.1175/MWR-D-17-0320.1

Wu, N., Ding, X., Wen, Z., Chen, G., Meng, Z., Lin, L., & Min, J. (2020). Contrasting frontal and warm-sector heavy rainfalls over South China during the early-summer rainy season. *Atmospheric Research*, *235*, 104693. https://doi.org/10.1016/j.atmosres.2019.104693

Xu, J., Bi, B., Chen, Y., Chen, T., Gong, Y., & Li, J. (2018). Mesoscale characteristics and mechanism analysis of the unexpected local torrential rain in Guangzhou on 7 May 2017. *Acta Meteorologica Sinica*, *76*(4), 511–524. (in Chinese with an English abstract). https://doi.org/10.11676/qxxb2018.016

Xu, J., Ma, Z., Yan, S., & Peng, J. (2022). Do ERA5 and ERA5-land precipitation estimates outperform satellite-based precipitation products? A comprehensive comparison between state-of-the-art model-based and satellite-based precipitation products over mainland China. *Journal of Hydrology*, *605*, 127353. https://doi.org/10.1016/j.jhydrol.2021.127353

Xu, W., Zipser, E. J., & Liu, C. (2009). Rainfall characteristics and convective properties of Mei-Yu precipitation systems over South China, Taiwan, and the South China Sea. Part I: TRMM observations. *Monthly Weather Review*, *137*(12), 4261–4275. https://doi.org/10.1175/2009MWR2982.1

Yu, S., Luo, Y., Wu, C., Zheng, D., Liu, X., & Xu, W. (2022). Convective and microphysical characteristics of extreme precipitation revealed by multisource observations over the Pearl River Delta at monsoon coast. *Geophysical Research Letters*, *49*(2), e2021GL097043. https://doi.org/10.1029/2021GL097043

Zhang, G. (2016). *Weather radar polarimetry* (p. 304). CRC Press.

Zhang, G., Vivekanandan, J., & Brandes, E. (2001). A method for estimating rain rate and drop size distribution from polarimetric radar measurements. *IEEE Transactions on Geoscience and Remote Sensing*, *39*(4), 830–841. https://doi.org/10.1109/36.917906

Zhang, R., Ni, Y., Liu, L., Luo, Y., & Wang, Y. (2011). South China heavy rainfall experiments (SCHeREX). *Journal of the Meteorological Society of Japan. Ser. II*, *89A*, 153–166. https://doi.org/10.2151/jmsj.2011-A10

Zhao, K., Huang, H., Wang, M., Lee, W.-C., Chen, G., Wen, L., et al. (2019). Recent progress in dual-polarization radar research and applications in China. *Advances in Atmospheric Sciences*, *36*(9), 961–974. https://doi.org/10.1007/s00376-019-9057-2

Zhong, S., Li, X., Yang, S., & Chen, Z. (2019). Characteristics and synoptic environment of torrential rain in the warm sector over South China: A composite study. *Meteorology and Atmospheric Physics*, *131*(5), 1191–1203. https://doi.org/10.1007/s00703-018-0629-y

Zhou, X., Xue, J., & Tao, Z. (2003). *Heavy rainfall experiment in South China during pre-summer rainy season (HUAMEX), 1998*. China Meteorological Press. (in Chinese). 220p.